THE JOURNAL OF PHYSICAL CHEMISTRY C

Article

Cite This: J. Phys. Chem. C 2020, 124, 1739−1748

pubs.acs.org/JPCC

Electrostatic Redox Reactions and Charge Storage in Molecular Electronic Junctions

Amin Morteza Najarian,[†] Mustafa Supur,[†] and Richard L. McCreery*

Department of Chemistry, University of Alberta, Edmonton, Alberta T6G 2R3, Canada

Supporting Information

ABSTRACT: The electronic properties of a molecular junction (MJ) consisting of a redox-active molecular layer and a 15 nm thick layer of aluminum oxide (AlOx) between conducting carbon contacts were compared to the same device lacking AlOx. For the electron acceptor naphthalene diimide (NDI), a negative bias applied to an NDI/AlOx MJ injects electrons into the NDI, which are blocked from further transport by the oxide. The electrons stored in the NDI more than double the charge storage over that of an equivalent dielectric parallel plate capacitor, and the dynamics of charging and discharging are completely distinct from those of a parallel plate. Replacement of NDI with an electron donor tetraphenylporphyrin (TPP) layer reverses the polarity of the charge/discharge process with electrons leaving the TPP layer under positive bias. The charge/discharge kinetics are temperature and bias dependent, indicating the electrons injected into the NDI layer result in nuclear reorganization to the configuration of an NDI^- anion. The devices exhibit electronic properties resembling a "dynamic chemical capacitor", in which carriers are stored in the molecular layer and the charging kinetics are controlled by reorganization energy, temperature, and applied bias. The molecule/oxide MJs are analogous to an electrochemical cell lacking ions, double layers, and solvent and involve only a single half reaction. In addition to providing kinetic information about basic electron transfer reactions underlying electrochemistry, electron donor−acceptor reactions, and electrostatic effects in organic electronics, the molecule/oxide MJs may have valuable applications in charge storage, memory, and as capacitors with a range of response times tunable by variations in structure and reorganization energy.

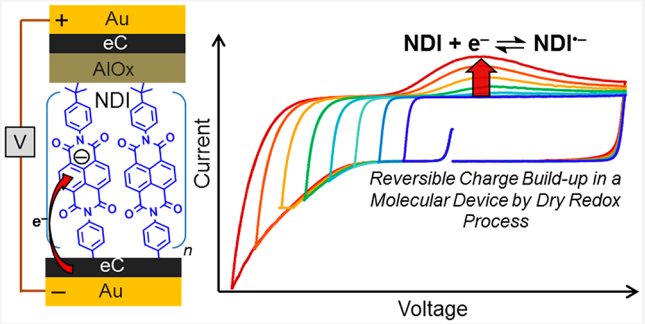

INTRODUCTION

Charge transport through single molecules or ultrathin (1−30 nm) molecular layers is the basis of molecular electronics, which seeks to realize new electronic functions for molecular devices which can augment silicon and conventional semiconductors. The molecular junction (MJ) consists of molecules oriented between conducting contacts and has been studied extensively with both single molecules and large ensembles, often covalently bonded to the contacts by a variety of techniques.[1−5] Transport across molecular dimensions (d) of 1−5 nm for aromatic molecules and 0.5−2 nm for alkanes is due to coherent quantum mechanical tunneling exhibiting an exponential dependence on charge transfer distance.[6] Beyond d = 5 nm, transport occurs via a series of "hopping" steps, which may involve finite residence time of the carrier in the molecular layer. For example, polarons formed in oligophenyleneimine molecules with d > 4 nm can cross a MJ via tunneling[7] or redox exchange,[8] and molecules containing redox centers can support transport over distances from 10 to 30 nm.[9−14] Although transport in MJs when d < 5 nm is generally accepted to involve coherent tunneling, the nature of the "sites" involved in hopping mechanisms (d > 5 nm) is unclear, as are the carrier residence time and the temperature dependence of MJ behavior.

A different aspect of MJs relates to device function and the identification of electronic properties unique to molecular components that are difficult or impossible with conventional semiconductors or may provide cost, power, or flexibility advantages which would support commercialization. Molecular tunnel junctions with d < 5 nm are available commercially, and their smooth, sigmoidal current−voltage (I−V) characteristics are useful for harmonic generation in electronic music equipment.[15] Charge storage in molecular junctions enables low-volatility memory applications,[16−18] including those based on conducting polymers.[19−21] To date, charge storage in MJs involves solvated mobile ions and two redox systems and is conceptually equivalent to a Faradaic electrochemical cell with charge transfer and electronic behavior dependent on ion motion and space charge compensation. In addition, redox states of molecules in reported single-molecule junctions have been observed only in liquid electrolytes.[22−27] In the current report, we describe electrolyte-free, dry MJs consisting of a 18−25 nm layer of donor or acceptor oligomers adjacent to a 15 nm redox-inert layer of disordered aluminum oxide (AlOx). The I−V characteristics of the molecule/oxide bilayer are

Received: December 12, 2019
Published: December 18, 2019

DOI: 10.1021/acs.jpcc.9b11515
J. Phys. Chem. C 2020, 124, 1739−1748

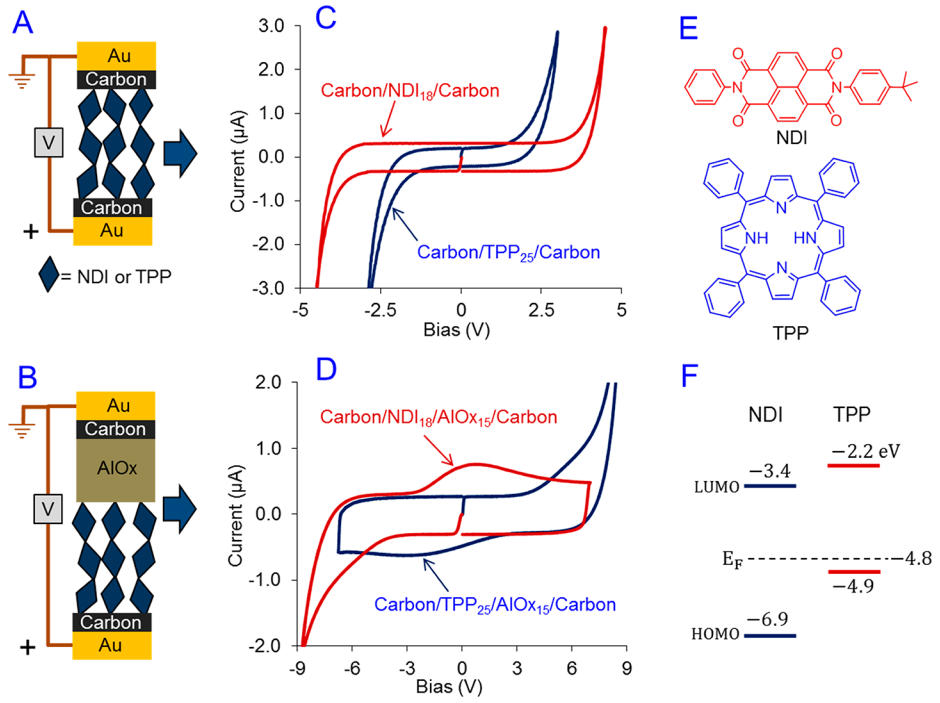

Figure 1. Schematic structures of (A) Au/C/molecule/C/Au and (B) Au/C/molecule/AlOx/C/Au junctions. (C) *I*−*V* responses for single layer NDI and TPP MJs. Active junction area is 0.00125 cm^2. (D) *I*−*V* responses for NDI and TPP MJs with the same thickness as in panel C, plus an additional 15 nm thick layer of AlOx. Bias values are stated as bottom electrode relative to top and are scanned at 1000 V/s. Subscripts in labels are layer thicknesses in nanometers. (E) Monomers of NDI and TPP layers with amino precursors shown in Figure S1. (F) HOMO and LUMO energies of NDI and TPP relative to vacuum calculated by DFT at the B3LYP/6-31G(d) level and Fermi level of e-beamed carbon from UPS.

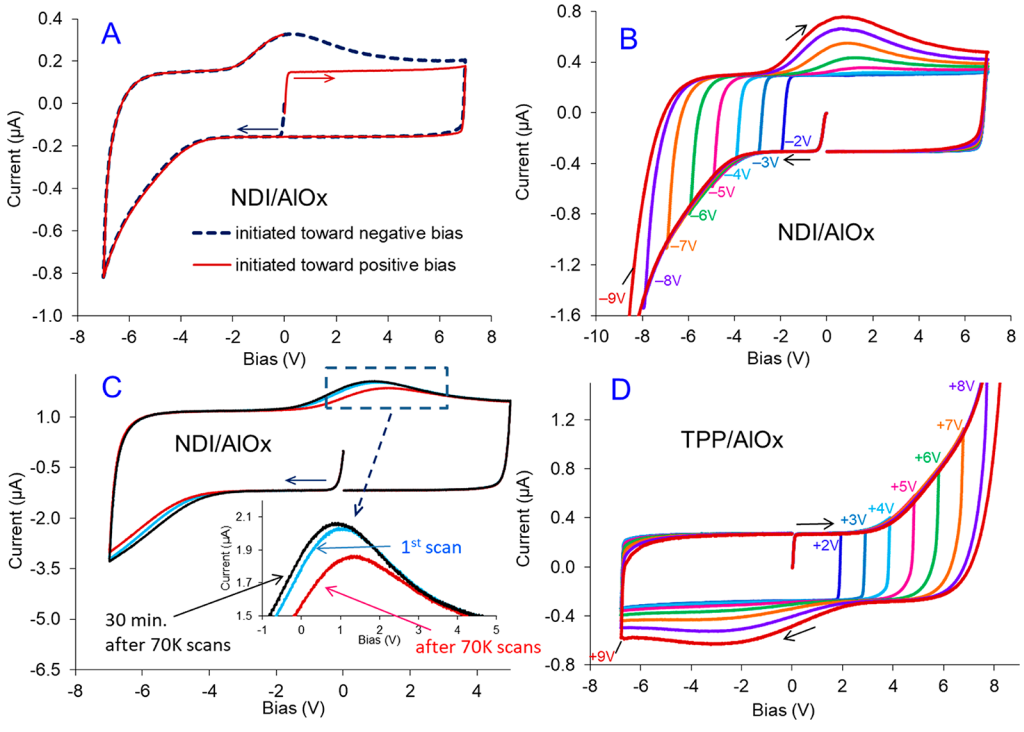

Figure 2. (A) Overlay of *I*−*V* cycles of NDI/AlOx junction initiated from 0 V initiated toward negative (dashed blue curve) and positive bias (solid red). (B) Overlay of *I*−*V* cycles of NDI(18 nm)/AlOx(15 nm) junction from 0 V toward indicated negative biases obtained under vacuum at 1000 V/s. (C) Overlay of *I*−*V* cycles of NDI(18 nm)/AlOx(15 nm) junction before (blue) and after (red) the 70 000 cycles in vacuum at 4000 V/s. Black curve was obtained after 30 min at open circuit. (D) Overlay of *I*−*V* cycles of TPP(25 nm)/AlOx(15 nm) junction from 0 V toward indicated positive biases obtained under vacuum at 1000 V/s.

completely distinct from those of the individual layers and provide unequivocal evidence that charge storage occurs in the molecular layer. In addition, nuclear reorganization accompanying electron transfer engenders dynamic, temperature

DOI: 10.1021/acs.jpcc.9b11515
J. Phys. Chem. C 2020, 124, 1739−1748

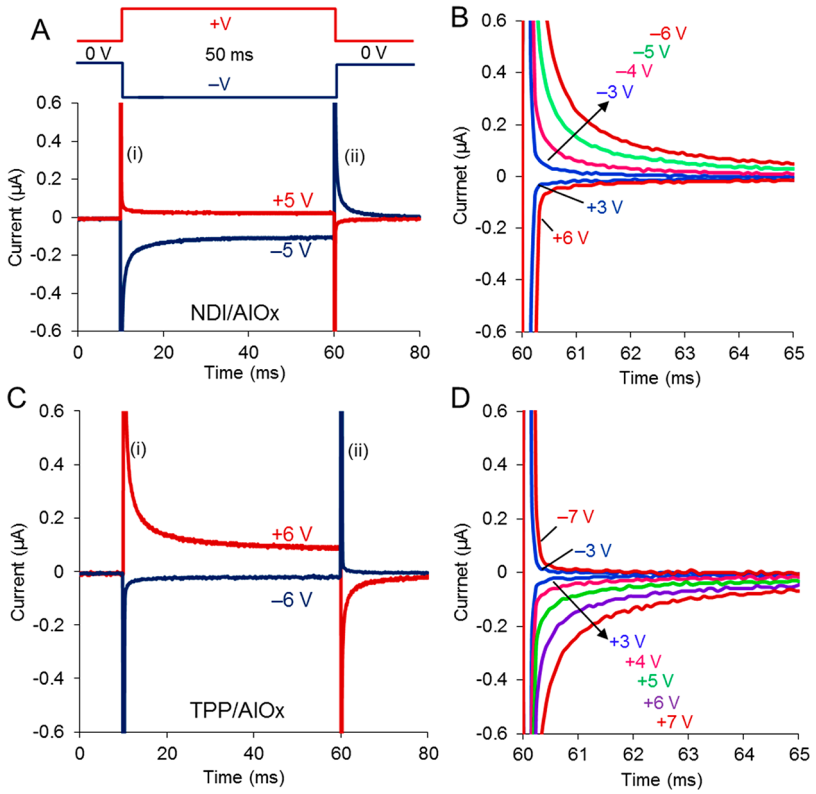

Figure 3. Left panel: Responses of NDI/AlOx (A) and TPP/AlOx (C) junctions to 50 ms bias pulses from 0 V to indicated voltages with charging (i) and discharging (ii) currents. Right panel: Discharge current responses of NDI/AlOx (B) and TPP/AlOx (D) junctions from indicated potentials to 0 V.

dependent capacitance clearly distinct from a conventional parallel plate capacitor and may have potential applications in delay lines and memory applications.

RESULTS AND DISCUSSION

Schematic drawings of MJs made with a naphthalene di-imide (NDI) derivative and tetraphenyl porphyrin (TPP) are shown in Figure 1A for single molecular layers and 1B for molecule/AlOx junctions with monomeric structures of the molecular layers shown in Figure 1E. The oligomers are grown by electrochemical reduction of the corresponding diazonium reagents made from the amino precursors shown in Supporting Information Figure S1 and are radical-mediated, resulting in covalent anchoring on very flat carbon electrodes. The Au, carbon (eC), and AlOx layers were deposited by electron-beam evaporation with the details of both molecular and e-beam procedures in the Supporting Information. Large-area molecular junctions made by diazonium reduction have proven reliable platforms for diverse molecular device applications[15,28−31] with high reproducibility of current vs bias (I–V) response and long lifetime reaching millions of I–V cycles, partly owing to covalent bonding between the molecules and contacts.[32−34] Figure 1F shows frontier energy levels for NDI and TPP monomers calculated from density functional theory relative to the Fermi level of eC,[33] all stated relative to the vacuum level.

Current vs bias (I–V) curves for $Au_{30}/eC_{10}/molecule/eC_{10}/Au_{20}$ MJs lacking AlOx are shown in Figure 1C for NDI (d = 18 nm) and TPP (d = 25 nm), scanned at 1000 V/s (subscripts are layer thicknesses in nanometers). Both show a constant parallel plate capacitor current near V = 0 and then an exponential increase due to conduction through the molecular layer at higher bias magnitude. Such behavior has been described previously[35−37] and is provided here for comparison to MJs containing AlOx. The red curve of Figure 1D shows an I–V scan at 1000 V/s for which the electrode adjacent to the NDI layer becomes increasingly negative to V = −9 V and then is returned to a constant positive bias of +7 V. The current between −3 and −9 V increases significantly over the constant current expected for a parallel plate capacitor and observed between 0 and −3 V. Note that the rapid increase in current for negative bias is qualitatively similar to that for an NDI MJ lacking AlOx (panel 1C) but that the positive portion of the I–V curve is completely different. A possibility explored in detail below is that electrons are injected into the NDI layer during the −3 to −9 V scan as was the case without AlOx present, but these electrons could not cross the AlOx barrier. When the NDI electron acceptor molecule was replaced with a TPP electron donor, the I–V response is completely reversed (1D, blue curve) with a large increase over a parallel plate response during positive bias scans and a broad peak at approximately −3 V on the reverse scan. This behavior is consistent with removal of electrons from the TPP HOMO during the positive scan, resulting in holes in the TPP layer which are refilled during the negative scan.

The unusual behavior of the molecule/AlOx MJs was investigated quantitatively with the results shown in Figure 2. If the scan is initiated toward positive bias for NDI/AlOx, the MJ behaves like a parallel plate capacitor (Figure 2A). Figure S2 shows that the current in the positive bias region is linear with scan rate, corresponding to a capacitance of 301 ± 2.3 pF over the 250 to 2000 V/s range. The positive current peak at ∼0 V

DOI: 10.1021/acs.jpcc.9b11515
J. Phys. Chem. C 2020, 124, 1739−1748

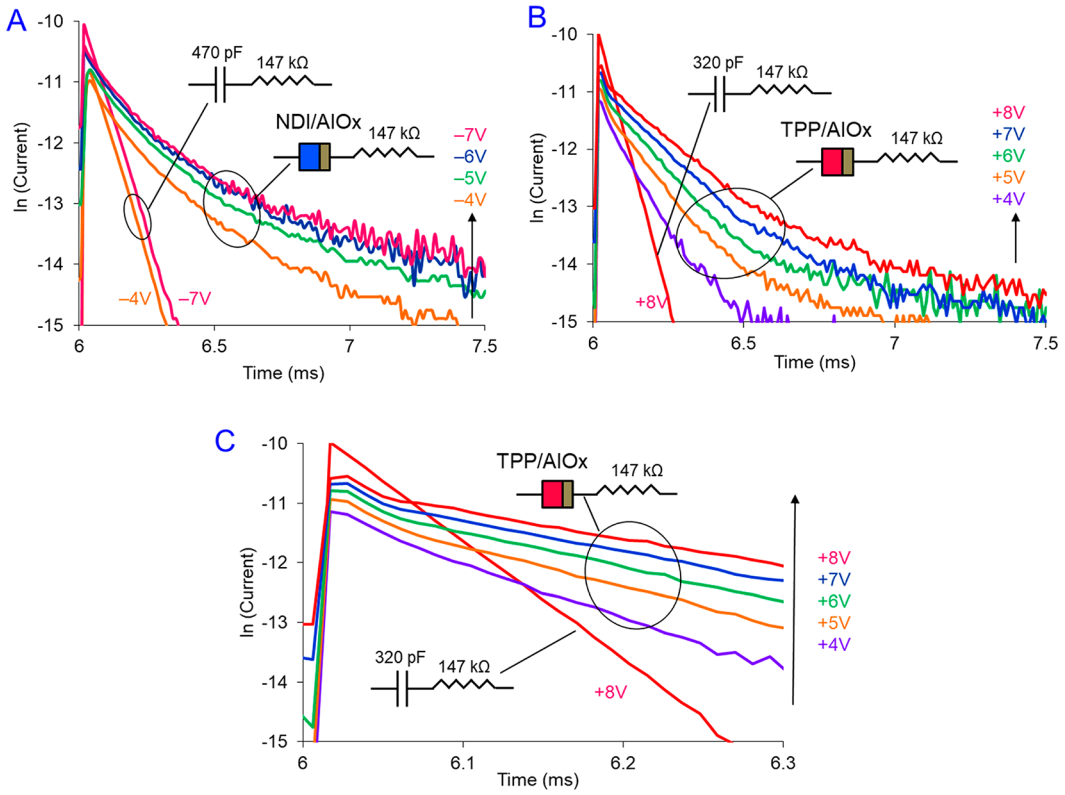

Figure 4. Discharge responses of molecule/AlOx molecular junction in series with a 147 kΩ resistor following a 5 ms pulse to the indicated bias and then return to $V = 0$ at $t = 6$ ms. (A) NDI/AlOx compared to a 470 pF capacitor in series with the same resistor. (B) TPP/AlOx junction compared to a 320 pF capacitor. (C) Enlargement of panel B for 6.0−6.3 ms discharge time. Transients were recorded in ambient air.

is observed only if the scan included sufficiently negative bias. Figure 2B shows a series of 1000 V/s scans to increasingly negative bias limits from −2 to −9 V, showing that the reverse peak size increases for the more negative bias limits. The integrated total negative charge under the curve for the −5 V scan was 3.81 nanocoulombs (nC), nearly equal to the total positive charge of 3.77 nC, indicating that most of the injected charge is recovered during the reverse scan. The ratio of positive to negative charge for scans to −4, −5, −6, and −7 V were 101, 99, 97, and 94%, respectively, with the decrease in recovery with more negative bias likely caused by leakage across the AlOx layer. For the −7 V scan of Figure 2B, the integrated charge for the positive scan is 5.51 nC, compared to 4.40 nC predicted for a conventional 300 pF capacitor. These observations are consistent with generation of NDI anions in the molecular layer with injected electrons returning to the bottom electrode during the peak-shaped $I-V$ response between −2 and +7 V. Figure 2C shows that the injection cycle may be repeated for 70 000 cycles at 4000 V/s between −7 and +5 V with minor changes in curve shape. The inset shows that the decrease in peak current is reversible with recovery of the initial response after 30 min at open circuit. The changes are likely due to residual charge in the molecular layer building up due to incomplete discharge during the positive scan. By analogy to a parallel plate capacitor, charge injection into the NDI layer decreases with the distance between the negative charge in the NDI electrode and the positive image charge on the electrode adjacent to AlOx, thus increasing overall capacitance. Figure 2D shows a series of $I-V$ curves to TPP/AlOx scanned at 1000 V/s to progressively more positive bias limits with responses similar to NDI/AlOx but with opposite polarity.

Bias voltage pulses can confirm the polarity and voltage dependence of charge injection and provide further dynamic information about electron transfer kinetics. Positive and negative pulses shown in Figure 3A lasting 50 ms were applied to the NDI/AlOx MJ with a return to zero bias after the voltage pulse. The current resulting from both $V = +5$ and −5 V pulses are shown in Figure 3A with polarity stated as the NDI electrode relative to the AlOx electrode. A +5 V pulse exhibits a fast RC spike decreasing to a nearly constant leakage current of ∼30 nA. Figure S3C shows a $\ln(I)$ vs time plot for a 100 μs pulse to +3 V, indicating an RC value for the spike of ∼30 μs, although the acquisition rate was too slow to yield an accurate value. The return to $V = 0$ at 60 ms has similar but opposite behavior and in both cases reflects the expected response of an ordinary parallel plate capacitor. A pulse to $V =$ −5 V yields very different behavior with larger currents both at the beginning and the end of the pulse and significantly slower decreases in current magnitude with time. An expansion of the return to $V = 0$ at 60 ms is shown in Figure 3B for increasingly negative pulse voltage and two positive pulses. All positive pulses returned rapidly to near zero current, while the negative pulses produced larger and longer-lasting current decays over ∼5 ms compared to the <0.1 ms for positive pulses. Plots of $\ln(I)$ vs time shown in Figure S4A for the discharge responses 60−70 ms of NDI/AlOx junctions were nonlinear, indicating a discharge behavior distinct from a conventional parallel plate capacitor. These decays are compared in more detail below, but an important point is that the larger positive currents following more negative pulses correspond to discharge of

DOI: 10.1021/acs.jpcc.9b11515
J. Phys. Chem. C 2020, 124, 1739−1748

electrons stored in the NDI layer as NDI^- anions during the negative pulse, confirming the scanning results of Figure 2B. In addition, the larger and nearly constant current at the end of the pulse for $V = -5$ V (−98 nA compared to +30 nA for $V = +5$ V) is likely due to leakage of the injected electrons across the AlOx layer. A TPP/AlOx junction exhibits similar behavior with opposite polarity, corresponding to removal of electrons from the TPP layer, i.e. the formation of cation species by positive pulses, which is apparently not accessible by the negative pulses (Figure 3C and D). Accordingly, currents corresponding to discharge of cation species in the TPP layer become larger for more positive pulses, validating the $I-V$ scans in Figure 2D, in which the discharge peak grows as more positive bias is applied.

The current response below 50 μs after pulse initiation was not well resolved with the current instrumentation, but the transient could be slowed by adding a 147 kΩ resistor (R) in series with the MJs, as shown in Figure 4A. The apparent capacitances for the MJ−R combinations were determined from the rectangular low bias region as shown in Figure S2, and the MJ−R devices were compared to a conventional capacitor having the same capacitance. Figure 4A shows semilogarithmic plots of discharge currents of junctions and their equivalent capacitors observed after 5 ms voltage pulses at selected potentials, with examples of the entire charge/discharge pulses provided in Figure S5. The 470 pF-147 kΩ circuit has the expected slope corresponding to RC = 70 μs for either −4 or −7 V pulses, while the NDI/AlOx-147 kΩ circuit has a nonlinear and much slower decay with a bias-dependent slope. The TPP/AlOx-147 kΩ combination has similar behavior for positive bias pulses with an apparently linear region between 6.1 and 6.5 ms showing a monotonic dependence of slope on bias voltage. Expansion of the 6.0−6.3 ms region for the TPP case is provided in Figure 4C, revealing a change in slope for the MJ−R case and a $V = -6$ V pulse from 69 to 175 μs. The initial slope for 6.0 to 6.1 ms is nearly equal to that observed for the time constant of the RC circuit, i.e. 51 μs. Beyond 6.1 ms, the slower decay for the MJ is likely due to reorganization of the NDI^- or TPP^+ radical ions after charge injection, resulting in an activation barrier for return to the uncharged state at room temperature. Note also that the decay rate past 6.1 ms is strongly dependent on pulse voltage, and preliminary experiments indicate it is also temperature dependent. In addition to providing kinetic information, the pulses permit comparison of charge storage in a simple capacitor to that in an MJ, via integration of the transients in Figure 4A and 4B. Q_{RC} in Table 1 is the observed charge under the discharge transient in Figure 4A for the 470 pF-147 kΩ RC circuit, while Q_{MJ-R} is the charge for the NDI/AlOx-147 kΩ combination. For increasingly negative bias pulses, Q_{RC} has the expected linear dependence on bias magnitude, while Q_{MJ-R} is nonlinear and significantly exceeds Q_{RC} by more than a factor of 2 for high pulse magnitudes. We define $Q_{Faradaic}$ as the excess charge stored in the MJ over that for the conventional RC circuit, i.e. $Q_{Faradaic} = Q_{MJ-R} - Q_{RC}$. As discussed below, electrons injected into the NDI layer can migrate to the NDI/AlOx interface under bias, effectively decreasing the distance between the electrons and their positive image charges in the AlOx electrode. A similar nonlinear trend is observed for a TPP/AlOx-147 kΩ circuit with $Q_{Faradaic}$ exceeding Q_{RC} obtained from a 320 pF-147 kΩ circuit when the positive pulse bias exceeds +7 V.

Table 1. Charge Storage from Discharge Responses of Junctions and Capacitors

$NDI_{18}/AlOx_{15}$				$TPP_{25}/AlOx_{15}$			
V_{pulse} (V)	Q_{RC} (nC)	Q_{MJ-R} (nC)	$Q_{Faradaic}$ (nC)	V (V)	Q_{RC} (nC)	Q_{MJ-R} (nC)	$Q_{Faradaic}$ (nC)
−4	1.9	4.0	2.1	+4	1.7	2.2	0.5
−5	2.3	5.8	3.5	+5	2.1	3.0	0.9
−6	2.8	7.3	4.5	+6	2.3	4.2	1.9
−7	3.3	8.1	4.8	+7	2.6	5.1	2.5
				+8	3.0	6.4	3.4
C, nF	0.47	1.38	0.91		0.31	1.05	0.74
C, μF/cm^2		1.10	0.73			0.84	0.59

The proposed injection of electrons into an NDI LUMO during negative bias excursions would likely be followed by nuclear reorganization because the electrons are trapped inside the NDI layer by the AlOx barrier. Reorganization would result in a temperature dependence of both injection and discharge which may differ significantly from that expected for classical Marcus redox kinetics. Figure 5A shows 1000 V/s scans on a NDI/AlOx MJ with slightly thicker layers than those used to make Figure 2. If the scan range is −3 to +7 V, the response is nearly rectangular with an apparent capacitance of 286 pF based on the parallel plate model. The minimal change in current or scan shape between 80 and 450 K implies that only electrons are moving without activation associated with nuclear motion. Figure 5B shows a wider scan range of ±7 V with a pronounced decrease in current with decreasing temperature, except for the +6 to 0 V portion attributable to a parallel plate. Magnification of the positive half of the voltammogram in Figure 5C shows changes in peak shape and position with temperature but also that the wave shape is nearly constant over the 80−200 K range. Integration of the current while scanning from −2 to +7 V provides the total discharge current (Q_{total}) following a scan to negative limit, V_{lim}, as shown in Figure 5D for $V_{lim} = -9$ V. Using the same integration range for different scan rates to $V_{lim} = -3$ to −9 V yielded Q_{total} plotted in Figure 6A for scan rates from 250 to 6000 V/s at 300 K. Q_{total} increases with a more negative V_{lim} and with slower scan rate, both of which are consistent with electron injection into NDI. Figure 6B shows Q_{total} for 1000 V/s scans over the 80−450 K temperature range and V_{lim}= −3, −5, −7, and −9 V vs $1000/T$, revealing a T-independent region below 200 K and an activated region above 200 K. Also shown is the Q_{total} observed for a 286 nF conventional parallel plate capacitor. For a negative limit of −3 V and $T < 250$ K, the capacitance of NDI/AlOx MJ is independent of temperature and stores the same charge as the 286 pF capacitor.

For more negative scan limits, Q_{total} increases with T and exceeds the parallel plate charge. Note also that charge storage is independent of T below 200 K but still significantly exceeds the parallel plate charge. $Q_{Faradaic}$ plotted in Arrhenius format in Figure 6C indicates near linearity for the T = 300−450 K range, and activationless below 200 K for V_{lim}= −5, −7, and −9 V with charge injection significantly above the parallel plate value even at T = 80 K. Furthermore, the apparent activation energies in the 300−450 K range shown in Figure 6D decrease linearly (R^2 = 0.985) with $E^{1/2}$ across the entire NDI/AlOx layer. The negligible Arrhenius slopes below 200 K imply that nuclear reorganization must follow or coincide with electron transfer but is not required preceding electron injection as would be the case for classical Marcus kinetics.

DOI: 10.1021/acs.jpcc.9b11515
J. Phys. Chem. C 2020, 124, 1739−1748

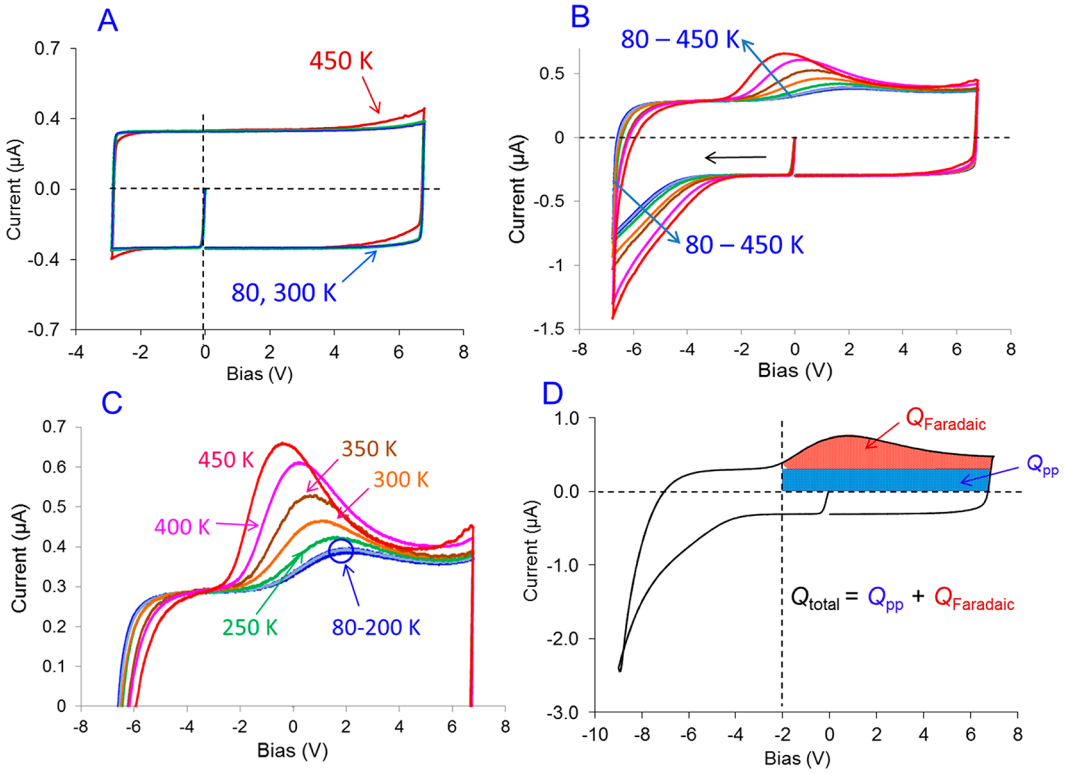

Figure 5. Voltammetry of an NDI/AlOx MJ in vacuum at 1000 V/s. (A) Scan limits of −3 and +7 V at 80, 300, and 450 K. (B) Initial scan to −7 V and then return to +7 V at 9 temperatures from 80 to 450 K. (C) Magnification of positive currents in panel B. (D) Integration of an IV scan with V_{lim} = −9 V to determine Q_{total}, Q_{pp}, and $Q_{Faradaic}$ for the portion of the positive scan between −2 to +7 V.

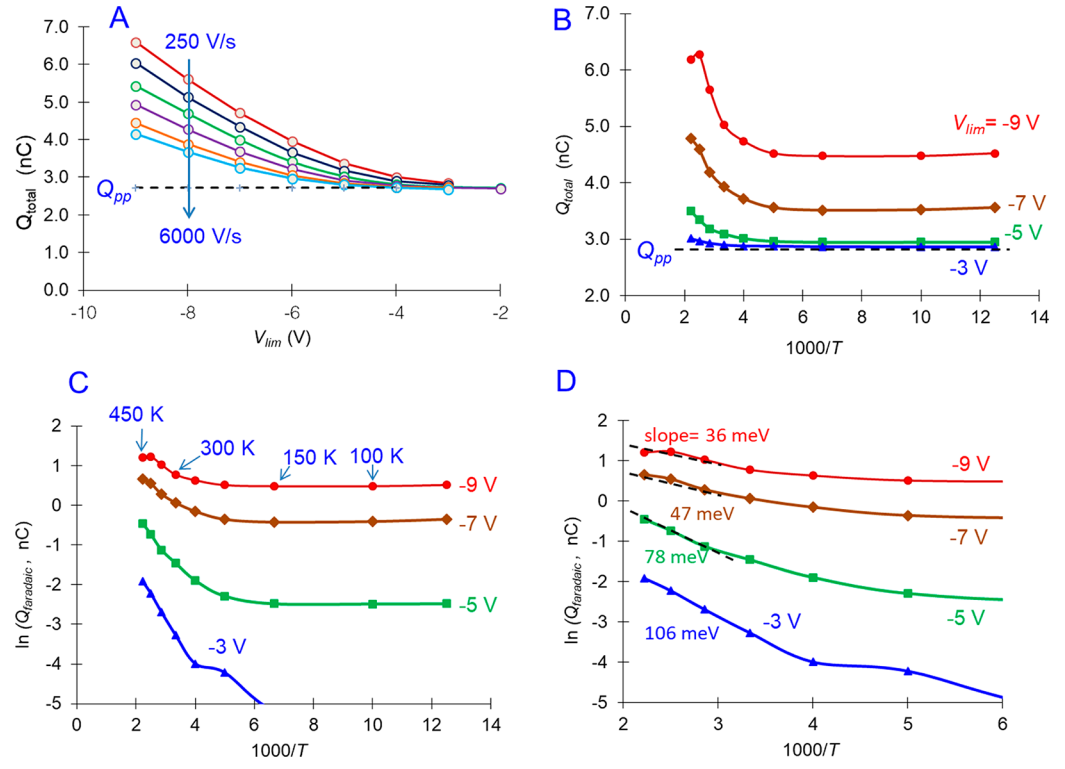

Figure 6. Total and Faradaic charge from −2 to +7 V for an NDI/AlOx junction determined as shown in Figure 5D. (A) Q_{total} as a function of V_{lim} and scan rate (250, 500, 1000, 2000, 4000, and 6000 V/s). Dashed line is Q_{total} for a conventional 286 pF capacitor. (B) Q_{total} vs inverse temperature for 1000 V/s scans to the indicated V_{lim}. (C) Natural log of $Q_{Faradaic}$ vs 1000/T, with $Q_{Faradaic} = Q_{MJ-R} - Q_{RC}$. (D) Expansion of panel C with apparent E_{act} indicated for each case over the T = 300−450 range.

DOI: 10.1021/acs.jpcc.9b11515
J. Phys. Chem. C 2020, 124, 1739−1748

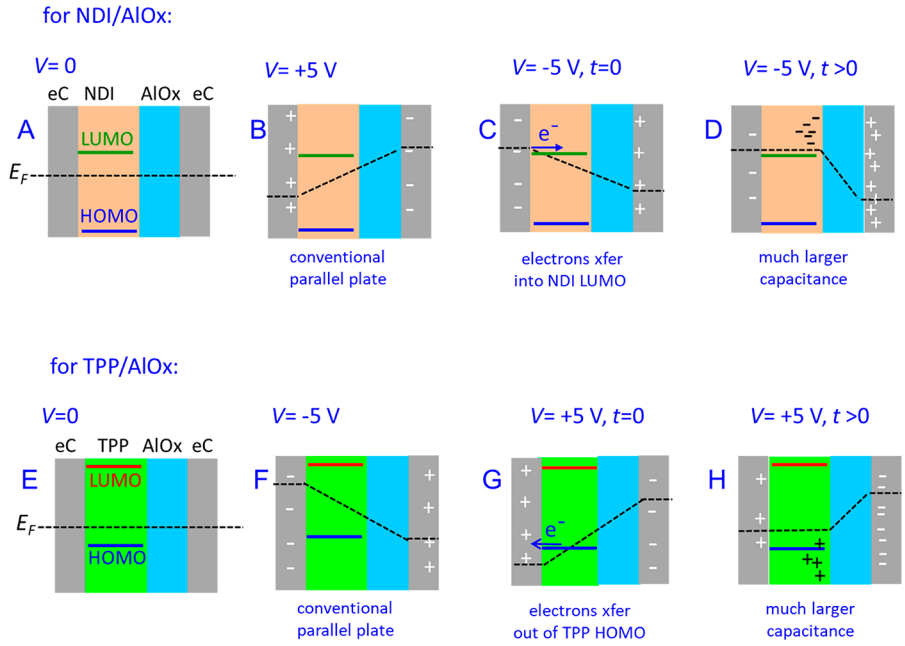

Figure 7. (A) Schematic energy levels in NDI/AlOx MJ relative to the carbon Fermi level, E_F (−4.8 eV relative to vacuum), at zero bias. (B) With +5 V bias applied to the NDI electrode; the dashed line indicating a linear potential profile through the molecular and oxide layers. (C) MJ immediately after a −5 V bias is applied, showing initiation of electron injection into the NDI LUMO. (D) Same device after migration of electrons to NDI/AlOx interface, increasing the electric field across the AlOx and device capacitance. (E−H) Similar events with opposite bias polarity for the case of the TPP electron donor. Energy shifts are estimates for illustration only, and nonlinear potential profiles are possible and likely in panels C, D, G, and H.

Although electrochemical reactions have been reported in molecular junctions,[20,27,38−41] organic thin film transistors,[42−45] and organic light emitting diodes,[46−48] quite distinct behavior is indicated in the NDI/AlOx and TPP/AlOx MJs by the lack of solvent, electrolyte ions, double layers, and counter reaction necessary for conventional electrochemistry. The absence of changes in electronic behavior after 70 000 cycles operating in a vacuum is not consistent with redox reactions of trace water or oxygen being involved in the observations because such reactions are expected to be chemically irreversible. A schematic of the proposed mechanism which is supported by the evidence is shown in Figure 7 with panel A representing an 18 nm layer of NDI and 15 nm of AlOx between two carbon electrodes having Fermi levels (E_F) at −4.8 V vs vacuum at zero bias. The HOMO and LUMO energies of NDI are shown with the LUMO being closer to E_F than the HOMO.

Figure 7B occurs after imposing a +5 V bias and assuming a linear potential profile through both the molecular and oxide layers. The simplified schematic does not reflect possible band bending or broadening, Fermi level pinning, interactions between the electrodes and molecules, and increased delocalization in an applied electric field. Electrons are prevented from entering the NDI LUMO from the right-hand electrode by the AlOx layer, which is too thick to permit tunneling. When the opposite −5 V bias is imposed (Figure 7C), electrons begin to inject into the LUMO but are prevented from traversing the AlOx layer because its orbitals are not energetically accessible. Transport across the NDI layer through its LUMO orbitals causes accumulation of electrons at the NDI/AlOx interface (Figure 7D) with an accompanying increase in capacitance due to the smaller distance between charged layers compared to that in Figure 7B. The positive image charge on the right electrode of Figure 7C is in addition to that present from the parallel plate capacitor, and the steeper potential profile reflects the higher electric field across the AlOx compared to that in Figure 7B. The electrons in the NDI layer are responsible for the increase in charge storage over that of the parallel plate for more negatively biased pulses, i.e. $Q_{Faradaic}$ in Table 1. The reorganization of NDI molecules near the AlOx interface to the nuclear coordinates of the NDI^- anion could be considered a Faradaic reduction, although there is no accompanying oxidation reaction or ion motion, and the image charge provides charge compensation. Return of the bias to $V = 0$ results in a reversal of the electric field across the NDI layer which drives electrons into the left electrode to produce the discharge pulses of Figure 4A. For the TPP/AlOx MJ case shown in Figure 7E−H, positive pulses extract electrons from TPP, and the resulting TPP^+ holes move toward the TPP/AlOx interface and are compensated by the negative image charge at the right electrode. Both electron injection into NDI and hole injection into TPP can be considered "redox" processes, albeit quite distinct from classical Faradaic reactions.

The effect of charge injection on capacitance can be assessed quantitatively from the observed capacitance values listed in Table 1. The discharge of a real 470 pF−147 kΩ RC combination yields an observed capacitance of 0.47 nF determined from the slope of Q vs V, which accurately reflects the expected charge stored in the capacitor. For an MJ−R combination with an MJ capacitance of 470 pF determined from voltammetry at low bias, the discharge following a 5 ms negative pulse is 0.84 $\mu F/cm^2$, based on the slope of Q vs V. For the d = 33 nm MJ, the apparent relative dielectric constant from the standard parallel plate model is $\varepsilon_r = 41$. This value is much higher than that for either Al_2O_3 ($\varepsilon_r \approx 10$) or aromatic molecules ($\varepsilon_r \approx 10$)[37] and physically unreasonable. However, if the charge separation is in fact ∼15 nm, as shown in Figure 7D, the apparent dielectric constant is $\varepsilon_r = 19$, and if only the

DOI: 10.1021/acs.jpcc.9b11515
J. Phys. Chem. C 2020, 124, 1739−1748

Faradaic capacitance of 0.73 $\mu F/cm^2$ is considered, the apparent dielectric constant is 12. Given the uncertainly in thicknesses (±1 nm) and differences between e-beam deposited AlOx and bulk Al_2O_3, the observed capacitance from discharge pulses agrees semiquantitatively with the values predicted from the mechanism depicted in Figure 7A–D. Analysis of discharge pulse data for TPP/AlOx yields similar results with the apparent ε_r decreasing from 38 for d = 40 nm to 14 for d = 15 nm.

The events depicted in Figure 7 have similarities to "electrostatic doping" in organic thin film transistors (TFTs), in which an image charge in a gate electrode is compensated by polarons in an organic semiconductor to modulate conductance in a channel between source and drain electrodes. TFT channels are generally a few micrometers wide, and doping must propagate into the channel by a series of electron transfers.[49,50] The current MJs have simpler, parallel plate geometry and much shorter transport distances of 18–25 nm, enabling redox events on a 10–100 μs time scale. Potential applications include a "dynamic chemical capacitor" in which the charge and discharge times can be varied by structural changes which vary the reorganization energy, and possibly local energy storage. The asymmetry of polarity apparent in Figure 3 is distinct from a parallel plate and will impart some rectification not present in conventional capacitors. The slow and tunable discharge rates of a chemical capacitor have some elements of the "memristor" which is widely studied and represents a distinct electronic component.[51−53]

CONCLUSION

Returning to the electrochemical analogy, the chemical capacitor is directly analogous to "dry electrochemistry" involving only one-half reaction, no corresponding counter reaction, no solvent, and no ion motion or ionic double layer. The chemical capacitor is "Faradaic" in that it involves electron transfer and nuclear reorganization, and the absence of solvent, ion motion, and a counter reaction may impart stability, indicated by the 70 000 redox cycles with slight and reversible changes in electronic response. The kinetic effects apparent in Figures 4 and 5 are of potentially broad interest because they represent a very simple form of electron transfer without solvent or ions. Understanding the fundamentals of charge transfer kinetics in molecule/oxide devices should be of interest in electrochemistry, electron donor–acceptor reactions, and electrostatic effects in solid-state organic electronic devices. Dry redox reactions and associated reorganization energy are factors not present in conventional microelectronics which may provide useful variables for rational design of molecular charge storage devices for memory applications and on-chip energy storage.

ASSOCIATED CONTENT

Supporting Information

The Supporting Information is available free of charge at https://pubs.acs.org/doi/10.1021/acs.jpcc.9b11515.

Fabrication and measurement procedures, additional I–V examples, and current responses to voltage pulses (PDF)

AUTHOR INFORMATION

Corresponding Author

*E-mail: mccreery@ualberta.ca.

ORCID

Amin Morteza Najarian: 0000-0002-0455-0451

Mustafa Supur: 0000-0003-2086-7106

Richard L. McCreery: 0000-0002-1320-4331

Author Contributions

†A.M.N. and M.S. contributed equally to the research.

Notes

The authors declare no competing financial interest.

ACKNOWLEDGMENTS

This work was supported by the University of Alberta, the National Research Council of Canada, the Natural Sciences and Engineering Research Council, and Alberta Innovates.

REFERENCES

(1) Jia, C.; Migliore, A.; Xin, N.; Huang, S.; Wang, J.; Yang, Q.; Wang, S.; Chen, H.; Wang, D.; Feng, B.; Liu, Z.; Zhang, G.; Qu, D.-H.; Tian, H.; Ratner, M. A.; Xu, H. Q.; Nitzan, A.; Guo, X. Covalently Bonded Single-Molecule Junctions with Stable and Reversible Photoswitched Conductivity. *Science* **2016**, *352*, 1443–1445.

(2) Choi, S. H.; Kim, B.; Frisbie, C. D. Electrical Resistance of Long Conjugated Molecular Wires. *Science* **2008**, *320*, 1482–1486.

(3) Kuang, G.; Chen, S.-Z.; Wang, W.; Lin, T.; Chen, K.; Shang, X.; Liu, P. N.; Lin, N. Resonant Charge Transport in Conjugated Molecular Wires Beyond 10 Nm Range. *J. Am. Chem. Soc.* **2016**, *138*, 11140–11143.

(4) Bonifas, A. P.; McCreery, R. L. "Soft" Au, Pt and Cu Contacts for Molecular Junctions through Surface-Diffusion-Mediated Deposition. *Nat. Nanotechnol.* **2010**, *5*, 612–617.

(5) Inkpen, M. S.; Liu, Z. F.; Li, H.; Campos, L. M.; Neaton, J. B.; Venkataraman, L. Non-Chemisorbed Gold–Sulfur Binding Prevails in Self-Assembled Monolayers. *Nat. Chem.* **2019**, *11*, 351–358.

(6) Amdursky, N.; Marchak, D.; Sepunaru, L.; Pecht, I.; Sheves, M.; Cahen, D. Electronic Transport *Via* Proteins. *Adv. Mater.* **2014**, *26*, 7142–7161.

(7) Taherinia, D.; Smith, C. E.; Ghosh, S.; Odoh, S. O.; Balhorn, L.; Gagliardi, L.; Cramer, C. J.; Frisbie, C. D. Charge Transport in 4 Nm Molecular Wires with Interrupted Conjugation: Combined Experimental and Computational Evidence for Thermally Assisted Polaron Tunneling. *ACS Nano* **2016**, *10*, 4372–4383.

(8) Smith, C. E.; Odoh, S. O.; Ghosh, S.; Gagliardi, L.; Cramer, C. J.; Frisbie, C. D. Length-Dependent Nanotransport and Charge Hopping Bottlenecks in Long Thiophene-Containing π-Conjugated Molecular Wires. *J. Am. Chem. Soc.* **2015**, *137*, 15732–15741.

(9) Sedghi, G.; Esdaile, L. J.; Anderson, H. L.; Martin, S.; Bethell, D.; Higgins, S. J.; Nichols, R. J. Comparison of the Conductance of Three Types of Porphyrin-Based Molecular Wires: B,Meso,B-Fused Tapes, Meso-Butadiyne-Linked and Twisted Meso-Meso Linked Oligomers. *Adv. Mater.* **2012**, *24*, 653–657.

(10) Sedghi, G.; Garcia-Suarez, V. M.; Esdaile, L. J.; Anderson, H. L.; Lambert, C. J.; Martin, S.; Bethell, D.; Higgins, S. J.; Elliott, M.; Bennett, N.; Macdonald, J. E.; Nichols, R. J. Long-Range Electron Tunnelling in Oligo-Porphyrin Molecular Wires. *Nat. Nanotechnol.* **2011**, *6*, 517–523.

(11) Sedghi, G.; Sawada, K.; Esdaile, L. J.; Hoffmann, M.; Anderson, H. L.; Bethell, D.; Haiss, W.; Higgins, S. J.; Nichols, R. J. Single Molecule Conductance of Porphyrin Wires with Ultralow Attenuation. *J. Am. Chem. Soc.* **2008**, *130*, 8582–8583.

(12) Tuccitto, N.; Ferri, V.; Cavazzini, M.; Quici, S.; Zhavnerko, G.; Licciardello, A.; Rampi, M. A. Highly Conductive 40-nm-Long Molecular Wires Assembled by Stepwise Incorporation of Metal Centres. *Nat. Mater.* **2009**, *8*, 41–46.

(13) Choi, S. H.; Frisbie, C. D. Enhanced Hopping Conductivity in Low Band Gap Donor/Acceptor Molecular Wires up to 20 Nm in Length. *J. Am. Chem. Soc.* **2010**, *132*, 16191–16201.

(14) Barraud, C.; Lemaitre, M.; Bonnet, R.; Rastikian, J.; Salhani, C.; Lau, S.; van Nguyen, Q.; Decorse, P.; Lacroix, J.-C.; Della Rocca, M.

DOI: 10.1021/acs.jpcc.9b11515
J. Phys. Chem. C 2020, 124, 1739–1748

L.; Lafarge, P.; Martin, P. Charge Injection and Transport Properties of Large Area Organic Junctions Based on Aryl Thin Films Covalently Attached to a Multilayer Graphene Electrode. *Nanoscale Advances* **2019**, *1*, 414−420.
(15) Bergren, A. J.; Zeer-Wanklyn, L.; Semple, M.; Pekas, N.; Szeto, B.; McCreery, R. L. Musical Molecules: The Molecular Junction as an Active Component in Audio Distortion Circuits. *J. Phys.: Condens. Matter* **2016**, *28*, 094011.
(16) Lindsey, J. S.; Bocian, D. F. Molecules for Charge-Based Information Storage. *Acc. Chem. Res.* **2011**, *44*, 638−650.
(17) Jiao, J.; Nordlund, E.; Lindsey, J. S.; Bocian, D. F. Effects of Counterion Mobility, Surface Morphology, and Charge Screening on the Electron-Transfer Rates of Porphyrin Monolayers. *J. Phys. Chem. C* **2008**, *112*, 6173−6180.
(18) Liu, Z.; Yasseri, A. A.; Lindsey, J. S.; Bocian, D. F. Molecular Memories That Survive Silicon Device Processing and Real-World Operation. *Science* **2003**, *302*, 1543−1545.
(19) Das, B. C.; Szeto, B.; James, D. D.; Wu, Y.; McCreery, R. L. Ion Transport and Switching Speed in Redox-Gated 3-Terminal Organic Memory Devices. *J. Electrochem. Soc.* **2014**, *161*, H831−H838.
(20) Kumar, R.; Pillai, R. G.; Pekas, N.; Wu, Y.; McCreery, R. L. Spatially Resolved Raman Spectroelectrochemistry of Solid-State Polythiophene/Viologen Memory Devices. *J. Am. Chem. Soc.* **2012**, *134*, 14869−14876.
(21) Lacaze, P. C.; Lacroix, J.-C. *Non-Volatile Memories*; ISTE Ltd: London, UK, 2014.
(22) Hosseini, S.; Madden, C.; Hihath, J.; Guo, S.; Zang, L.; Li, Z. Single-Molecule Charge Transport and Electrochemical Gating in Redox-Active Perylene Diimide Junctions. *J. Phys. Chem. C* **2016**, *120*, 22646−22654.
(23) Li, Y.; Baghernejad, M.; Qusiy, A.-G.; Zsolt Manrique, D.; Zhang, G.; Hamill, J.; Fu, Y.; Broekmann, P.; Hong, W.; Wandlowski, T.; Zhang, D.; Lambert, C. Three-State Single-Molecule Naphthalenediimide Switch: Integration of a Pendant Redox Unit for Conductance Tuning. *Angew. Chem., Int. Ed.* **2015**, *54*, 13586−13589.
(24) Darwish, N.; Díez-Pérez, I.; Da Silva, P.; Tao, N.; Gooding, J. J.; Paddon-Row, M. N. Observation of Electrochemically Controlled Quantum Interference in a Single Anthraquinone-Based Norbornylogous Bridge Molecule. *Angew. Chem., Int. Ed.* **2012**, *51*, 3203−3206.
(25) Li, X. L.; Hihath, J.; Chen, F.; Masuda, T.; Zang, L.; Tao, N. J. Thermally Activated Electron Transport in Single Redox Molecules. *J. Am. Chem. Soc.* **2007**, *129*, 11535−11542.
(26) Haiss, W.; van Zalinge, H.; Higgins, S. J.; Bethell, D.; Hobenreich, H.; Schiffrin, D. J.; Nichols, R. J. Redox State Dependence of Single Molecule Conductivity. *J. Am. Chem. Soc.* **2003**, *125*, 15294−15295.
(27) Wang, Z.; Dong, H.; Li, T.; Hviid, R.; Zou, Y.; Wei, Z.; Fu, X.; Wang, E.; Zhen, Y.; Nørgaard, K.; Laursen, B. W.; Hu, W. Role of Redox Centre in Charge Transport Investigated by Novel Self-Assembled Conjugated Polymer Molecular Junctions. *Nat. Commun.* **2015**, *6*, 7478.
(28) Najarian, A. M.; McCreery, R. L. Long-Range Activationless Photostimulated Charge Transport in Symmetric Molecular Junctions. *ACS Nano* **2019**, *13*, 867−877.
(29) Chandra Mondal, P.; Tefashe, U. M.; McCreery, R. L. Internal Electric Field Modulation in Molecular Electronic Devices by Atmosphere and Mobile Ions. *J. Am. Chem. Soc.* **2018**, *140*, 7239−7247.
(30) Tefashe, U. M.; Nguyen, Q. V.; Lafolet, F.; Lacroix, J.-C.; McCreery, R. L. Robust Bipolar Light Emission and Charge Transport in Symmetric Molecular Junctions. *J. Am. Chem. Soc.* **2017**, *139*, 7436−7439.
(31) Saxena, S. K.; Smith, S. R.; Supur, M.; McCreery, R. L. Light-Stimulated Charge Transport in Bilayer Molecular Junctions for Photodetection. *Adv. Opt. Mater.* **2019**, *7*, 1901053.
(32) Supur, M.; Van Dyck, C.; Bergren, A. J.; McCreery, R. L. Bottom-up, Robust Graphene Ribbon Electronics in All-Carbon Molecular Junctions. *ACS Appl. Mater. Interfaces* **2018**, *10*, 6090−6095.
(33) Morteza Najarian, A.; Szeto, B.; Tefashe, U. M.; McCreery, R. L. Robust All-Carbon Molecular Junctions on Flexible or Semi-Transparent Substrates Using "Process-Friendly" Fabrication. *ACS Nano* **2016**, *10*, 8918−8928.
(34) Yan, H.; Bergren, A. J.; McCreery, R. L. All-Carbon Molecular Tunnel Junctions. *J. Am. Chem. Soc.* **2011**, *133*, 19168−19177.
(35) Yan, H.; Bergren, A. J.; McCreery, R.; Della Rocca, M. L.; Martin, P.; Lafarge, P.; Lacroix, J. C. Activationless Charge Transport across 4.5 to 22 Nm in Molecular Electronic Junctions. *Proc. Natl. Acad. Sci. U. S. A.* **2013**, *110*, 5326−5330.
(36) Sayed, S. Y.; Fereiro, J. A.; Yan, H.; McCreery, R. L.; Bergren, A. J. Charge Transport in Molecular Electronic Junctions: Compression of the Molecular Tunnel Barrier in the Strong Coupling Regime. *Proc. Natl. Acad. Sci. U. S. A.* **2012**, *109*, 11498−11503.
(37) Bergren, A. J.; McCreery, R. L.; Stoyanov, S. R.; Gusarov, S.; Kovalenko, A. Electronic Characteristics and Charge Transport Mechanisms for Large Area Aromatic Molecular Junctions. *J. Phys. Chem. C* **2010**, *114*, 15806−15815.
(38) Bonifas, A. P.; McCreery, R. L. Solid State Spectroelectrochemistry of Redox Reactions in Polypyrrole/Oxide Molecular Heterojunctions. *Anal. Chem.* **2012**, *84*, 2459−2465.
(39) Nowak, A. M.; McCreery, R. L. In Situ Raman Spectroscopy of Bias-Induced Structural Changes in Nitroazobenzene Molecular Electronic Junctions. *J. Am. Chem. Soc.* **2004**, *126*, 16621−16631.
(40) Leary, E.; Higgins, S. J.; van Zalinge, H.; Haiss, W.; Nichols, R. J.; Nygaard, S.; Jeppesen, J. O.; Ulstrup, J. Structure-Property Relationships in Redox-Gated Single Molecule Junctions; a Comparison of Pyrrolo-Tetrathiafulvalene and Viologen Redox Groups. *J. Am. Chem. Soc.* **2008**, *130*, 12204−12205.
(41) Xiao, X.; Brune, D.; He, J.; Lindsay, S.; Gorman, C. B.; Tao, N. Redox-Gated Electron Transport in Electrically Wired Ferrocene Molecules. *Chem. Phys.* **2006**, *326*, 138−143.
(42) Kim, C.-H.; Frisbie, C. D. Field Effect Modulation of Outer-Sphere Electrochemistry at Back-Gated, Ultrathin Zno Electrodes. *J. Am. Chem. Soc.* **2016**, *138*, 7220−7223.
(43) Xia, Y.; Frisbie, C. D. Low-Voltage Electrolyte-Gated OTFTs and Their Applications. In *Organic Electronics II*; Wiley-VCH Verlag GmbH & Co. KGaA: 2012; pp 197−233.
(44) Xia, Y.; Cho, J.; Paulsen, B.; Frisbie, C. D.; Renn, M. J. Correlation of on-State Conductance with Referenced Electrochemical Potential in Ion Gel Gated Polymer Transistors. *Appl. Phys. Lett.* **2009**, *94*, 013304.
(45) Natali, D.; Caironi, M. Charge Injection in Solution-Processed Organic Field-Effect Transistors: Physics, Models and Characterization Methods. *Adv. Mater.* **2012**, *24*, 1357−1387.
(46) Handy, E. S.; Pal, A. J.; Rubner, M. F. Solid-State Light-Emitting Devices Based on the Tris-Chelated Ruthenium(II) Complex. 2. Tris(Bipyridyl)Ruthenium(II) as a High-Brightness Emitter. *J. Am. Chem. Soc.* **1999**, *121*, 3525−3528.
(47) Kalyuzhny, G.; Buda, M.; McNeill, J.; Barbara, P.; Bard, A. J. Stability of Thin-Film Solid-State Electroluminescent Devices Based on Tris(2,2'-Bipyridine)Ruthenium(II) Complexes. *J. Am. Chem. Soc.* **2003**, *125*, 6272−6283.
(48) Buda, M.; Kalyuzhny, G.; Bard, A. J. Thin-Film Solid-State Electroluminescent Devices Based on Tris(2,2'-Bipyridine)-Ruthenium(II) Complexes. *J. Am. Chem. Soc.* **2002**, *124*, 6090−6098.
(49) Panzer, M. J.; Frisbie, C. D. High Carrier Density and Metallic Conductivity in Poly(3-Hexylthiophene) Achieved by Electrostatic Charge Injection. *Adv. Funct. Mater.* **2006**, *16*, 1051−1056.
(50) Kaake, L. G.; Zou, Y.; Panzer, M. J.; Frisbie, C. D.; Zhu, X. Y. Vibrational Spectroscopy Reveals Electrostatic and Electrochemical Doping in Organic Thin Film Transistors Gated with a Polymer Electrolyte Dielectric. *J. Am. Chem. Soc.* **2007**, *129*, 7824−7830.
(51) Lee, M.-J.; Lee, C. B.; Lee, D.; Lee, S. R.; Chang, M.; Hur, J. H.; Kim, Y.-B.; Kim, C.-J.; Seo, D. H.; Seo, S.; Chung, U. I.; Yoo, I.-K.; Kim, K. A Fast, High-Endurance and Scalable Non-Volatile Memory Device Made from Asymmetric Ta_2O_{5-x}/TaO_{2-x} Bilayer Structures. *Nat. Mater.* **2011**, *10*, 625−630.

DOI: 10.1021/acs.jpcc.9b11515
J. Phys. Chem. C 2020, 124, 1739−1748

(52) Strachan, J. P.; Pickett, M. D.; Yang, J. J.; Aloni, S.; Kilcoyne, A. L. D.; Medeiros-Ribeiro, G.; Williams, R. S. Direct Identification of the Conducting Channels in a Functioning Memristive Device. *Adv. Mater.* **2010**, *22*, 3573−3577.
(53) Yang, J. J.; Pickett, M. D.; Li, X.; Ohlberg, D.; Stewart, D.; Williams, R. S. Memristive Switching Mechanism for Metal/Oxide/Metal Nanodevices. *Nat. Nanotechnol.* **2008**, *3*, 429−433.

DOI: 10.1021/acs.jpcc.9b11515
J. Phys. Chem. C 2020, 124, 1739−1748